ORIGINAL PAPER

High-quality dense ZnO thin films: work function and photo/electrochemical properties

H. Krysova[1,2] · V. Mansfeldova[1] · H. Tarabkova[1] · A. Pisarikova[2] · Z. Hubicka[2] · L. Kavan[1]

Abstract

Compact ZnO (wurtzite) thin films are prepared on four different substrates by (i) spray pyrolysis or (ii) pulsed reactive magnetron sputtering combined with a radio frequency electron cyclotron wave resonance plasma. Films are characterized by AFM, XRD, Kelvin probe, cyclic voltammetry, electrochemical impedance spectroscopy, and UV photoelectrochemistry. Film morphologies, defect concentrations, crystallite size, and orientation provided specific fingerprints for the electronic structure of ZnO close to the conduction band minimum. Fabricated films are referenced, if relevant, to a model system based on a wurtzite single crystal with either Zn-face or O-face termination. Kelvin probe measurements of the ZnO/air interface distinguished effects of annealing and UV excitation, which are attributed to removal of oxygen vacancies close to the surface. In turn, the work function, at the electrochemical interface, specifically addressed the growth protocol of the ZnO electrodes but not the effects of crystallinity and annealing. Finally, high photocurrents of water oxidation are observed exclusively on virgin films. This effect is then discussed in terms of photocorrosion, and work function changes due to UV light.

Introduction

Zinc oxide is a popular functional material for applications ranging from large scale industrial usage to advanced opto-electronic, spintronic, and piezoelectronic devices [1]. ZnO is a direct band-gap semiconductor exhibiting n-type conductivity with high carrier mobilities ($\approx$100 cm^2 V^{-1} s^{-1}). Also, p-doping of ZnO has been reported; however, it remains elusive [1]. ZnO nanomaterials and thin films are useful for photovoltaics (both dye-sensitized [2] and perovskite [3] solar cells), antimicrobial applications [4], Li-ion batteries [5], photoelectrochemical water splitting [6–8], and photocatalysis [9]. For photoelectrochemical and photovoltaic applications, these films are typically deposited on conductive substrates, e.g., F-doped SnO$_2$ (FTO) or indium-tin oxide (ITO).

The rational use of ZnO thin films and electrodes requires knowledge of the electronic structure, particularly near the conduction band minimum. For this, the archetypal experimental approach consists of determination of the flatband potential and donor concentration by Mott-Schottky analysis, based on electrochemical impedance spectroscopy (EIS) of the semiconductor/electrolyte-solution interface. However, due to the fact that this analysis is often carried out on unsuitable (e.g., nano-porous) material, together with an oversimplified experimental approach [10, 11], reports in the literature are inconsistent [12].

Determination of work function and its tuning is essential for applications of ZnO in many areas. While numerous studies [13–15] describe the effect of doping on work function, we demonstrate that ZnO work function is also affected by film thickness, preparation method, and post-deposition treatment. Furthermore, the flatband potentials of ZnO thin films are reported to be almost pH-independent, which is a striking anomaly as compared to various other oxide semiconductors, e.g., TiO$_2$ and SnO$_2$, and even compared to the single-crystal ZnO (wurtzite) [12]. This behavior was tentatively attributed to the fact that one abundant crystal face on ZnO (wurtzite) is capped either by O atoms, (000$\bar{1}$), or by

✉ L. Kavan
kavan@jh-inst.cas.cz

1 J. Heyrovsky Institute of Physical Chemistry, Czech Academy of Sciences, Dolejskova 3, 18223 Prague 8, Czech Republic

2 Institute of Physics, Czech Academy of Sciences, Na Slovance 2, 18200 Prague 8, Czech Republic

Zn atoms, (0001), and these faces exhibit different surface polarity [16]. However, detailed studies of work functions of these faces are still missing.

Morphological issues associated with polycrystalline thin films on conductive substrates are particularly appealing [12]. These studies require a selection of syntheses, which can produce perfect non-porous dense films. They must be impermeable to electrolyte solutions, which is manifested by blocking of charge transfer reactions on the underlying conductive substrate. A quality test based on suitable redox systems, such as $Fe(CN)_6^{3-/4-}$, $Ru(bpy)_3^{3+/2+}$, $Ru(NH_3)_6^{3+/2+}$, or $spiro$-OMeTAD$^{2+/0}$, demonstrates rectifying behavior on good films, i.e., a solely cathodic charge-transfer with no anodic counterpart in cyclic voltammograms. Representative data are available for TiO_2 [17–19] or SnO_2 [17, 20]; however, ZnO thin films have not been characterized at this level yet. Except for a very brief note in [21], Mott-Schottky analysis was made on films, which were not deliberately tested for their blocking behavior. This presents a challenge for targeted optimization of the synthetic protocol to grow ZnO thin films of this quality.

The second general issue is the fact that the flatband potential and the corresponding work function (position of the Fermi level with respect to vacuum) are not material constants but complex variables depending primarily on the environment surrounding the investigated surface [22]. Model studies of TiO_2 single crystal electrodes revealed that, for fundamental reasons, work function measured by EIS, photoelectron spectroscopy (UPS, XPS), or Kelvin probe can vary over a broad range of nearly 1 eV [22]. This finding is corroborated by the density functional theory (DFT) calculations for adsorption of molecular and dissociated water on the TiO_2 surface [23, 24]. More specifically, these calculations elucidate the environment-borne variations of the work functions in anatase/rutile TiO_2 [24].

Also, the effect of film crystallinity needs to be considered. A comparison of quasi-amorphous and crystalline thin films indicated that the crystallinity effect on the work function was small, or negligible in TiO_2 [19], but very significant in SnO_2 [19, 20, 25–27]. In the latter case, enhancement of the work function amounted to ca. 0.3–0.5 eV following thermal crystallization, as indicated by Kelvin probe [19], UPS [25, 26], and electrochemical [20, 27] studies. To date, there is no similar study of ZnO thin films, therefore providing another motivation for this work.

ZnO thin films are often prepared by plasmatic methods. The low-temperature plasma contains ions and electrons with specific concentrations and energetic distributions [28]. This type of plasma is used, *inter alia,* for surface treatment of various semiconducting oxides [29]. Recently, ZnO and ZnO:Al films were prepared by magnetron sputtering of a ceramic ZnO target at different conditions, and their optical and electrical properties were studied [30]. The ZnO films

prepared by radio frequency (RF) reactive magnetron sputtering from Zn metallic target and ZnO ceramic target in $Ar + O_2$ gas mixture were presented, e.g., in [31].

The current paper describes an original method for fabrication of ZnO thin films using a new hybrid physical vapor deposition (PVD) source combining reactive pulse sputtering of Zn metallic target and the radio frequency electron cyclotron wave resonance (ECWR) plasma. To the best of our knowledge, this technique is used here for the first time to grow ZnO thin films. For comparison, we synthesized the ZnO thin films by a more common method of spray pyrolysis too. In both cases, the deposition conditions were optimized to grow high-quality (pinhole-free) thin films.

This study employs an array of characterization methods: X-ray diffraction (XRD), atomic force microscopy (AFM), Kelvin probe (KP), and several photo/electrochemical techniques. It allowed for concerted investigation of relations between synthesis, structure, and properties of ZnO thin films. The photoelectrochemical studies are addressing open problems of the efficiency of photon-to-electron conversion. More specifically, ZnO thin films are unique because the classical diffusion-drift (Gärtner) model is insufficient to describe their photoelectrochemical behavior [32]. The deviations were attributed to the unusually large exciton binding energy ($\approx$60 meV), causing long-range backward diffusion of excitons in the ZnO/electrolyte interface [32]. The current paper further discloses interestingly high photocurrents, which are observed in all virgin films, independent of their synthetic history.

Experimental section

Materials and electrodes

FTO glass (TEC-8, Dyesol) was cleaned ultrasonically in ethanol (96%), acetone, and isopropyl alcohol. These solvents were of analytical grade quality, purchased from Penta Chemicals Unlimited. Flat (100) Si/SiO_2 with 300 nm SiO_2 (Silicon Quest International, USA) were used for AFM studies. Pure Si substrates (without SiO_2) were from UniversityWafer, Inc. USA. The amorphous SiO_2 substrates were purchased from UVC Servis, s.r.o., Czech Republic. SiO_2 substrates are denoted by "Q" to avoid the problematic term "*optical quartz glass*." ZnO single crystal ($5\times5\times0.5$ mm^3; wurtzite (0001)/(000$\overline{1}$) orientation) was from SurfaceNet, GmbH (Germany).

Thin films were deposited by spray pyrolysis (SP) [33] in air using a solution of 0.1 M Zn-acetate + 0.1 M ammonium acetate in 2-methoxyethanol, with a substrate temperature of 350 °C. The optimal deposition protocol consisted of repeated cycles of spraying of ca. 50 mL aerosol with 1 min relaxation time between cycles. Layer thickness was

controlled by the number of spray cycles (from 25 to 100) and determined by ellipsometry or AFM profile analysis of a step formed on a Si/SiO_2 substrate following removal of the ZnO film by scratching (cf. Figure S1 in Supporting Info). Four samples were prepared with average ZnO-layer thicknesses of approximately 35 nm (SP1), 65 nm (SP2), 105 nm (SP3), and 120 nm (SP4).

Alternatively, ZnO thin films were deposited by a combination of pulsed reactive magnetron sputtering (MS) and radio frequency ECWR plasma. This deposition method was previously used for the deposition $CuFeO_2$ [34], Fe_2O_3 [35], and TiO_2 [36]. A circular planar magnetron with a pure zinc (99.99%) target (50-mm diameter and 6-mm thickness) was reactively sputtered in an $Ar + O_2$ gas mixture. The gas flow of argon was $Q_{Ar} = 15$ sccm, and of oxygen was $Q_{O2} = 10$ sccm, with a gas pressure $p = 0.3$ Pa. A pulsed frequency $f_p = 40$ kHz was used for the magnetron discharge excitation, and an RF power supply with frequency 13.56 MHz and power $P_{RF} = 200$ W was used for ECWR plasma generation. Substrates were heated during the deposition process to 300 °C. Three samples were prepared in this way with layer thicknesses of 35 nm (MS1), 75 nm (MS2), and 110 nm (MS3). Thicknesses were determined using the same methods as for the SP films. For subsequent heat treatment, if relevant, the as-grown films were annealed for 1 h in air at 450 °C; the heating ramp was 5 °C/min.

Non-electrochemical methods

X-ray diffraction (XRD) was measured using an Empyrean diffractometer (Malvern Panalytical) with CuKα radiation (wavelength, $\lambda = 0.154$ nm), in a grazing incidence configuration with an incidence angle of 1 deg and a step size of 0.02 deg. The crystallite size (coherent domain size), D, was calculated from the full width at half-maximum height (FWHM) using the Scherrer formula:

$$D = \frac{K \cdot \lambda}{\beta_w \cdot cos\theta} \tag{1}$$

K is a constant related to crystallite shape (here, $K = 0.9$); β_w is the peak width (in radians) of the diffraction peak profile at half-maximum height (FWHM), and θ is the diffraction angle. The diagnostic reflection (0002) of ZnO wurtzite ($2\theta \approx 34$ deg) was used for the analysis.

Kelvin probe measurements were carried out in air using a KP020 instrument (KP Technology Ltd). A gold probe was positioned close to the sample surface, and contact potential difference was measured. Electrical connection to the sample surface was made by indium tape. Work functions were calibrated using freshly peeled-off highly oriented pyrolytic graphite, with work function set to 4.6 eV [37]. In some cases, samples were illuminated by UV light (365 nm, 6 W/cm²,

Bluepoint LED lamp, Hönle UV Technology) for 10 min. Morphology of films was characterized by tapping mode atomic force microscopy (AFM) (Dimension Icon, Bruker, USA) with a silicon cantilever VTESPA-300 (resonant frequency ≈ 300 kHz, spring constant $k = 42$ N/m, nominal tip radius 5 nm, Bruker, USA). Gwyddion software (v. 2.53) was utilized for processing of AFM image data. Surface roughness is expressed by the roughness factor (R_f) and the roughness average (R_a). R_f is a ratio of the three-dimensional surface area and the two-dimensional footprint area of the image. R_a is defined as the arithmetic average of absolute values of the surface height deviations (Z_j) measured from the mean plane according to equation:

$$R_a = \frac{1}{N} \sum_{j=1}^{N} \left| Z_j \right| \tag{2}$$

Roughness parameters (R_f, R_a) were calculated from AFM-height (5×5 μm²) images.

Electrochemical methods

An Autolab 302N potentiostat (Metrohm) equipped with a frequency response analyzer was used for cyclic voltammetry (CV) and EIS studies. The counter electrode was a platinum wire (Metrohm 6.0301.100). The homemade Pt mesh electrode 1×1 cm² (Goodfellow 0.06 mm wire dia, 82×82 wires/in) was used for impedance measurements. The reference electrode was Ag/AgCl (3 M KCl) from Metrohm (WOC SGJ 60724140). The electrolyte solution was 0.5 M KCl saturated with ZnO; its pH was between 5.4 and 5.9 (pH Meter 913 from Metrohm). To account for casual pH fluctuations, potentials in all electrochemical measurements were recalculated, quoting the reversible hydrogen electrode (RHE) as a reference. In accord with a general practice, the Nernstian pH-dependence (−59 mV/pH) is assumed for the RHE potential [12, 38]. However, for the analysis of flatband potentials, the ZnO-specific pH-dependence is assumed, viz., −4.8 mV/pH for ZnO thin films and −67 mV/pH for single crystals, respectively [12]. All electrochemical measurements were made in an Ar atmosphere.

Electrochemical impedance spectroscopy was investigated over a frequency range from 100 kHz to 0.1 Hz (modulation amplitude 10 mV) at varying potentials. Spectra were evaluated using Zview (Scribner) software by fitting to a Randles-type circuit. Here, R_{CT} is the charge-transfer resistance, which is parallel to constant phase element (CPE) to account for non-ideal capacitive behavior [17, 18, 20, 22]. The impedance of CPE equals [10, 19, 22]

$$Z_{CPE} = B^{-1}(i\omega)^{-\beta} \tag{3}$$

with ω being the EIS circular frequency and B (admittance pre-factor) and β (exponent) are the frequency-independent

parameters of the CPE ($0.8 \leq \beta \leq 1$; experimental values were from 0.8 to 0.9). The interfacial capacitance, C, is calculated from:

$$C = \frac{(R_{CT} \cdot B)^{1/\beta}}{R_{CT}} \qquad (4)$$

The source data (R_{CT}, B, and β) were determined by fitting of the complete impedance spectra (measured at each applied potential from 100 kHz to 0.1 Hz) [10, 12, 17].

Photoelectrochemical measurements were performed under Ar in 0.5 M Na_2SO_4 solution saturated with ZnO (pH 7). The cell was equipped with a fused silica optical window. The photoelectrochemical cell was placed in a dark room and controlled by a Zahner workstation. Films were illuminated from the front side by a 365-nm UV LED diode (LS365-2, Zahner) with an intensity of 10 mW/cm^2. Photoexcitation

was applied with 5 s dark/light intervals. Electrolytes, solvents, and other chemicals were of standard quality (p.a. or electrochemical grade) purchased from Aldrich or Merck. Figure 1 shows schematically the complete procedure of film preparation and characterization.

Results and discussion

Structural studies by AFM and XRD

Figure 2 shows the nanomorphology of ZnO films with medium thickness ($\approx$ 70 nm) fabricated by spray pyrolysis (SP2) or by magnetron sputtering (MS2). Reference images of blank substrates are presented in Fig. S2 (Supporting Info). AFM-height images demonstrate the uniform polycrystalline texture of dense films deposited by

Fig. 1 Flow chart of all performed synthetic procedures and characterization methods
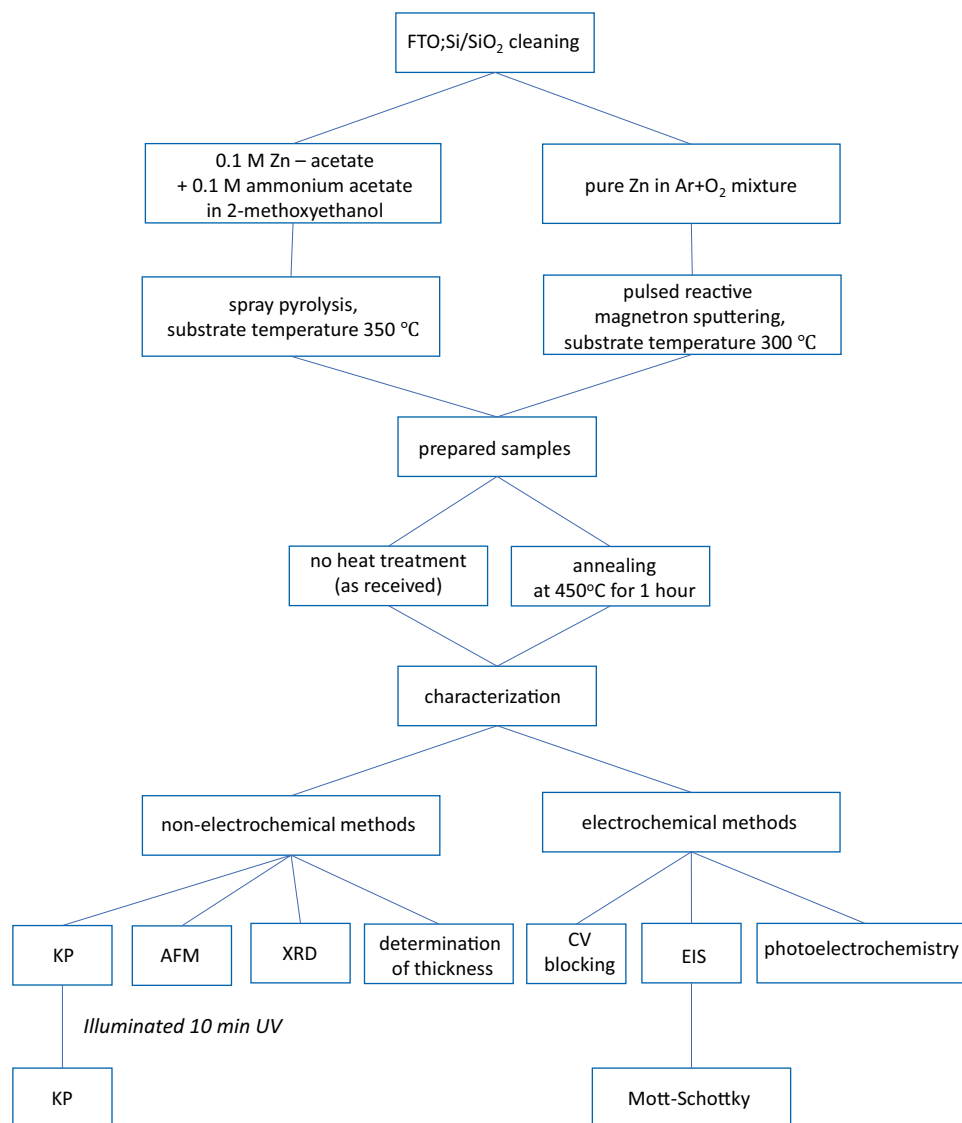
Fig. 2 AFM images of ZnO films produced by spray pyrolysis (SP2, 65 nm) and magnetron sputtering (MP2, 70 nm) on various substrates. **A** SP2 films on flat Si/SiO$_2$, **B** MP2 film on flat Si/SiO$_2$, **C**, **E** SP2 films on FTO, and **D**, **F** MP2 films on FTO. **A**–**D** are AFM height images. **E**, **F** are AFM phase images. Black bars represent 500 nm
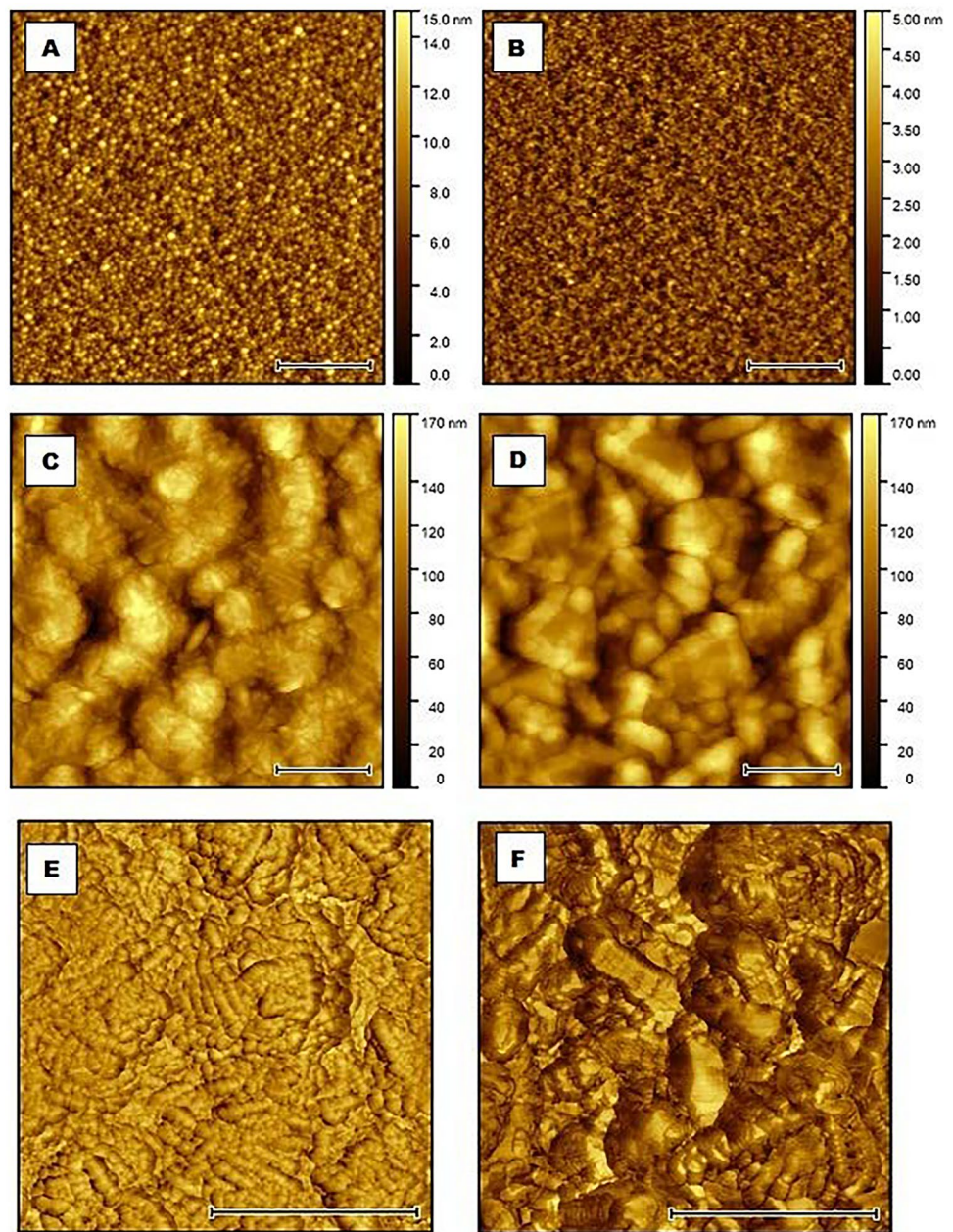
both techniques on flat substrates (Si/SiO$_2$) (Fig. 2A, B; cf. Fig. S2B). A roughness average, R_a, of 0.4 nm was found for MS2 film, whereas SP2 film showed a higher roughness average, by a factor of 4–5, ($R_a = 1.8$ nm), the latter also exhibited larger ZnO nanograins. Table 1 summarizes the calculated R_a and R_f parameters for all samples.

The overall surface structure of FTO-supported thin films is, as expected, related to the FTO support (Fig. 2C–F and Fig. S2A). This quantitatively confirms that R_a values, which range between 30 to 33 nm, are independent of the sample nature, i.e., SP@FTO, MS@FTO, or blank FTO (Table 1). The roughness factors, R_f, of blank FTO is 1.26, which agrees with earlier studies [20, 39, 40]. The coverage

of FTO by ZnO films seems to be more homogenous for the spray-pyrolyzed process, although the surface roughness is like that of magnetron-sputtered films (Fig. 2C, D).

XRD patterns in Fig. 3 confirm a hexagonal wurtzite structure for all films. To minimize perturbations caused by substrates, diffractograms of the thickest films, MS3 and SP4 ($\approx$110–120 nm), are presented. Practical applications of ZnO [2, 3] and other [17, 20] oxide thin films, e.g., in photovoltaics, often require post-annealing (typically at 450 °C in air for 1 h) which, reportedly, improves crystallinity and removes carbonaceous impurities from previous preparative steps. Hence, we also show in Fig. 3 diffractograms of annealed ZnO films.

Table 1 Roughness factors, R_f, and average roughness, R_a, for ZnO films produced by spray pyrolysis (SP1-SP4) and magnetron sputtering (MS1-MS3) on FTO and Si/SiO$_2$ substrates. All roughness parameters were calculated from AFM height (5×5 μm^2) images. Reference data for uncoated substrates are also shown

Film	R_f @ FTO	R_a @ FTO [nm]	R_f @ Si/SiO$_2$	R_a @ Si/SiO$_2$ [nm]
SP1	1.28	33	1.02	1.8
SP2	1.24	33	1.02	1.8
SP3	1.29	32	1.07	3.9
SP4	1.26	30	1.03	3.1
MS1	1.30	31	-	-
MS2	1.27	30	1.00[a]	0.4
MS3	1.21	31	1.00[a]	0.5
Si/SiO$_2$ (reference)	-	-	1.00[a]	0.2
FTO (reference)	1.26	32	-	-

[a]Difference of surface and projected area is within statistical errors ($\ll 1\%$)

Table 2 lists crystallite sizes, D, calculated from the Scherrer formula (Eq. 1). Following annealing, D values increase for MS3 films but remain virtually unchanged for SP4 films. This could be due to a higher deposition temperature (350 °C instead of 300 °C) for the as-received (as-rec) SP4 samples and their less pronounced orientation (see below). Crystallite sizes (from 12 to 26 nm) are much larger than the surface roughness of flat supports, which are in the Å range, cf. Table 1. This shows that the fabricated ZnO films have a high-quality compact morphology. Crystal sizes are comparable to the thickness for SP1 and MS1 films (35 nm). More specifically, all films (thicknesses 35–120 nm) appear to consist of only $\approx$2–10 monolayers of single crystallites, which, nevertheless perfectly sinter into a pinhole-free thin film (except for the SP1 film, see below).

Detailed analysis of XRD patterns (Fig. 3) reveals the significant preferential orientation of films, deposited by magnetron sputtering on amorphous SiO$_2$ (Q) and Si substrates, independent of post-annealing. In both cases, the
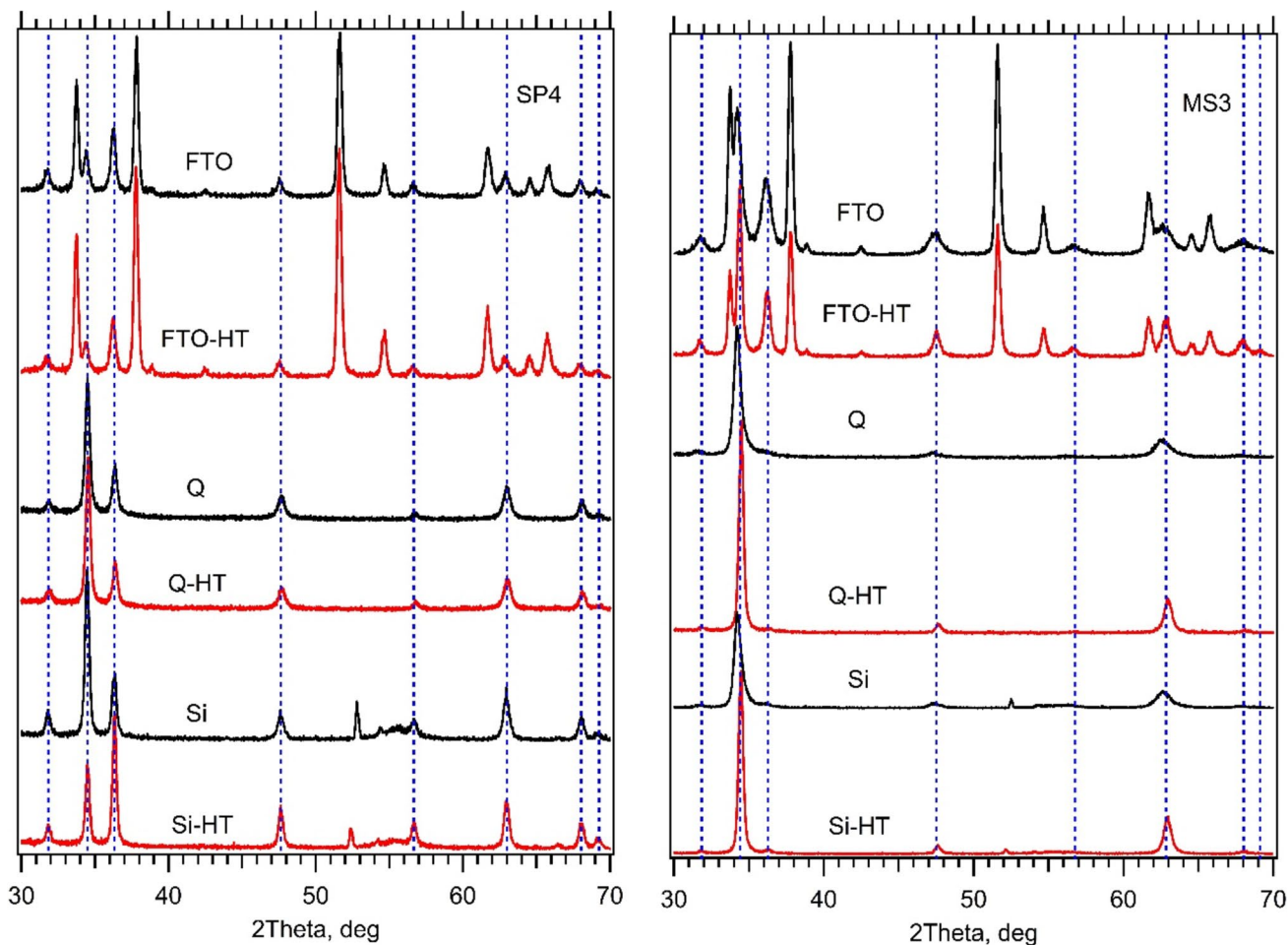
Fig. 3 X-ray diffraction patterns of ZnO films on various substrates: FTO, amorphous SiO$_2$ (Q) and Si. The symbol HT indicates heat treatment in air at 450 °C for 1 h (red line). Left chart shows diffrac- tograms of SP4 film; right chart shows diffractograms of MS3 film. Dashed lines mark the main peaks of ZnO wurtzite

Table 2 XRD peak shift (2θ), FWHM, and crystallite size (D) for (0002) ZnO thin films on three different substrates (FTO, Si, Q) as-deposited samples and samples annealed at 450 °C (HT). Q denotes amorphous SiO_2 substrate (see Experimental Section)

| | Reflection (0002) | | | | | |
| | As-deposited | | | HT (450 °C) | | |
	Peak shift (2θ) [deg]	FWHM [deg]	D [nm]	Peak shift (2θ) [deg]	FWHM [deg]	D [nm]
MS3 @ FTO	34.18	0.718	12	34.36	0.336	25
MS3 @ Si	34.24	0.554	15	34.44	0.354	23
MS3 @ Q	34.20	0.394	21	34.47	0.354	23
SP4 @ FTO	34.38	0.372	22	34.36	0.382	22
SP4 @ Si	34.44	0.315	26	34.44	0.315	26
SP4 @ Q	34.47	0.315	26	34.47	0.315	26

diffractogram is dominated by the (0002) peak at ≈ 34.5 deg (2θ) and by the (10$\bar{1}$3) peak at ≈ 63 deg; however, features at ≈ 32 and ≈ 36.5 deg, assigned to (10$\bar{1}$0) and (10$\bar{1}$1) diffractions of ZnO wurtzite, respectively, are strongly attenuated. A preferred orientation of crystallites is often observed for ZnO thin films prepared by reactive sputtering methods [41–43]. This effect also occurs in other materials (Fe_2O_3 and TiO_2) prepared by the hybrid system of pulsed sputtering and ECWR plasma [35, 36]. Currently, it is assumed that crystal orientation in these sputtering methods is dependent on the substrate material, temperature, kinetic energy of sputtered particles, intensity, and energetic distribution of ion-bombardment of the substrate during the growth process [35, 36, 41]. Čada et al. [41] also presents reference diffraction intensities of randomly-oriented hexagonal polycrystalline ZnO.

In general, the significant preferential orientation, observed for MS3 films on Si and amorphous SiO_2 (Q), is not reproduced for films produced by spray pyrolysis (SP4) on any substrate. In this case, all expected diffraction lines for wurtzite are detected, though with varying intensities, where relative intensities change with substrate type and presence/absence of heat treatment. When comparing SP4 and MS3 films on FTO, a preferential (0002)-orientation for MS3 on FTO is clear. In this case, it is proposed that the anisotropic nature of spray-pyrolyzed films is responsible for the uniform decoration of FTO grains as opposed to magnetron-sputtered films, which keep preferential orientation along the c-axis, including on FTO (cf. AFM and XRD data in Figs. 2 and 3, respectively).

Figure 3 further confirms the presence of the FTO-related peaks in all relevant plots for both samples, i.e. SP4 and MS3 on the FTO substrates (FTO and FTO-HT; the symbol HT means heat treatment). Other impurities are not detectable, except for weak features between 52 and 56 deg, which are assigned to SiO_2 cristobalite on Si-supported films. Cristobalite is apparently formed by air oxidation of Si during film growth. As expected, its signal is stronger in the SP4 film, which was grown by spray pyrolysis in air, as opposed to the MS3 film, which was grown in vacuum with a small O_2 concentration (see Experimental Section for details).

Electrochemical methods (CV and EIS)

As mentioned in the "Introduction", dense films are mandatory for their proper characterization using, e.g., the EIS [12]. The cyclic voltammetry of the $Fe(CN)_6^{3-/4-}$ redox couple was used as quality test (Fig. 4). ZnO films grown by spray pyrolysis (SP2-SP4) exhibit almost ideal rectifying behavior, i.e., reduction of ferricyanide at potentials negative to ca. 0.4 V vs. RHE is selectively enabled, but reverse anodic oxidation of ferrocyanide, even at highly positive potentials, is completely blocked. Only the thinnest film (SP1; 35 nm) contains some pinholes, which can be classified as "defect B." In this defect, voltammetric peaks, attributed to a reaction on the supporting FTO, appear, albeit, with larger peak-to-peak splitting [17]. From corresponding peak currents, a relative pinhole area of 22% for SP1 film can be estimated, whereas this value is $\approx 1\%$ for the remaining thicker SP-films (Fig. 4, left chart).

Interestingly, thicker ZnO films (SP2-SP4) keep their good blocking function even after thermal annealing at 450 °C. This is reminiscent of the behavior of SnO_2 [20] and some (but not all [17]) TiO_2 [19] thin films fabricated by atomic layer deposition (ALD). However, spray-pyrolyzed TiO_2 films usually contain a large proportion of defects in the as-received state and are very sensitive to subsequent cracking following heat treatment [17]. ZnO produced by magnetron sputtering (MS1-3) exhibits a good blocking function for $Fe(CN)_6^{3-/4-}$ redox couple in all investigated thicknesses (35–110 nm), and this behavior is not much impaired by annealing (Fig. 4 right chart). Deeper inspection of cyclic voltammograms (Fig. 4) reveals a somewhat stronger sensitivity to cracking for MS1-3 films, as opposed to SP2-4 films. It is tempting to propose that this is caused by the pronounced thermal growth of crystallites in MS-films, compared to the crystallites in SP-films, which are virtually unaffected by annealing (see Fig. 3, Table 2 and discussion thereof).

For MS films, relative pinhole areas are from 1 to 3%. Hence, selected thin films (SP2-4 and MS1-3) are of appropriate quality to be investigated by Mott-Schottky analysis, to determine the flatband potential (V_{fb}), work function (φ_{fb}),
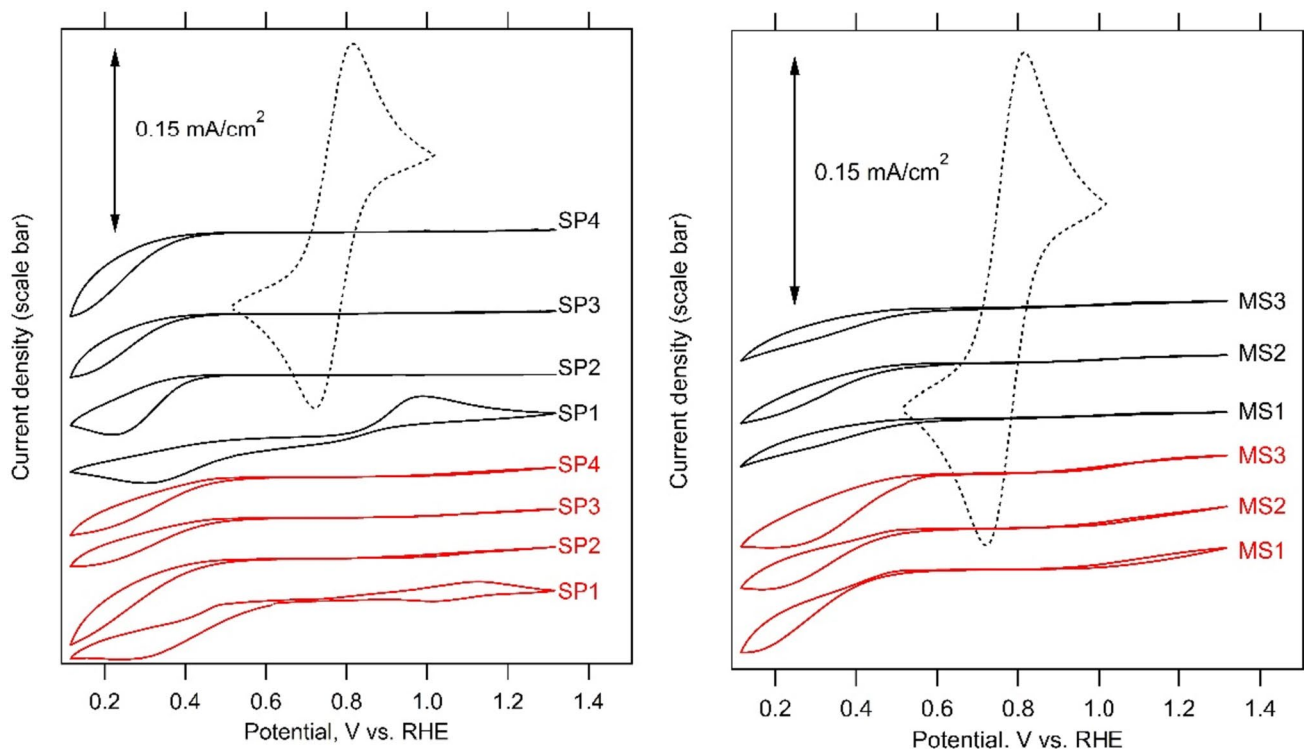
Fig. 4 Cyclic voltammogram of an uncoated FTO electrode (dashed line) and coated by ZnO thin films either by spray pyrolysis (left chart) or by magnetron sputtering (right chart). Black lines indicate as-prepared films; red lines indicate the same film following heat treatment at 450 °C for 1 h. Scan rate 50 mV/s. Electrolyte solution is 0.5 mM $K_4Fe(CN)_6 + 0.5$ mM $K_3Fe(CN)_6$ in aqueous 0.5 M KCl saturated with ZnO. Voltammograms are offset for clarity. Current density scale is the same for all voltammograms

and donor concentration (N_D) in well-defined conditions [12]. Fitting of a complete impedance spectrum (measured from 100 kHz to 0.1 Hz) is used here. The fit is further processed to get the interfacial capacitance (*C*) from *CPE* (see Experimental section). Though in certain cases (e.g., in amorphous thin films), the single-frequency measurements provide useful information too [44]; the deconvolution of complete EIS-spectrum is a robust evaluation method, which is generally preferable for the high-quality crystalline thin film and single crystal electrodes [10]. Figures 5 and 6 show Mott-Schottky plots from electrochemical impedance spectroscopy of all films. The linear parts of the plots tend to grow with layer thickness and can be described by the equation:

$$\frac{1}{C^2} = \left(\frac{2}{e\varepsilon_0\varepsilon_r N_D}\right)\left(V_{app} - V_{fb} - \frac{k_B T}{e}\right) + \frac{1}{C_H^2} \quad (5)$$

e is the electron charge, ε_0 is the permittivity of free space, ε_r is the dielectric constant (ε_r value for ZnO is 7.8 [7]), V_{app} is the applied potential, k_B is the Boltzmann constant, and *T* is temperature. The Helmholtz capacitance, C_H, is assumed to be in the order of tens of μF/cm^2 [45], i.e., much larger than the space-charge capacitance and consequently causing negligible contribution to Eq. 5. The second approximation

consists of assuming the AFM-determined roughness factor for the calculation of capacitance (*C*). More specifically, the roughness factor (R_f) from atomic force microscopy (Table 1) is used for correcting the projected electrode areas.

Within these approximations, the flatband potential is close to 0.2 V vs. RHE for all ZnO films produced by spray-pyrolysis and close to 0.3 V vs. RHE for all ZnO films deposited by magnetron sputtering. In all cases, the effect of annealing is small, if any. Individual values are collated in Table 3. It should be noted that a comprehensive statistical analysis (223 complied entries) by Patel et al. [12] showed that the most common value for V_{fb} was 0.203 V vs. RHE (despite the spread of literature data exceeding 1 V). Zhang et al. [46] reported V_{fb} values of 0.20 or 0.23 V vs. RHE for the O-terminated or Zn-terminated, (000$\bar{1}$) or (0001), respectively, faces of single crystal ZnO (wurtzite). These values are in good agreement with flatband potentials reported here (Table 3). Therefore, it is reasonable to say that films investigated here behave as high-quality semiconductor electrodes. Small fluctuations in V_{fb} values reported in Table 3 are caused by experimental and fitting errors (e.g., pH effect of referencing potentials against RHE). Consistently lower flatband potential values are observed for films produced
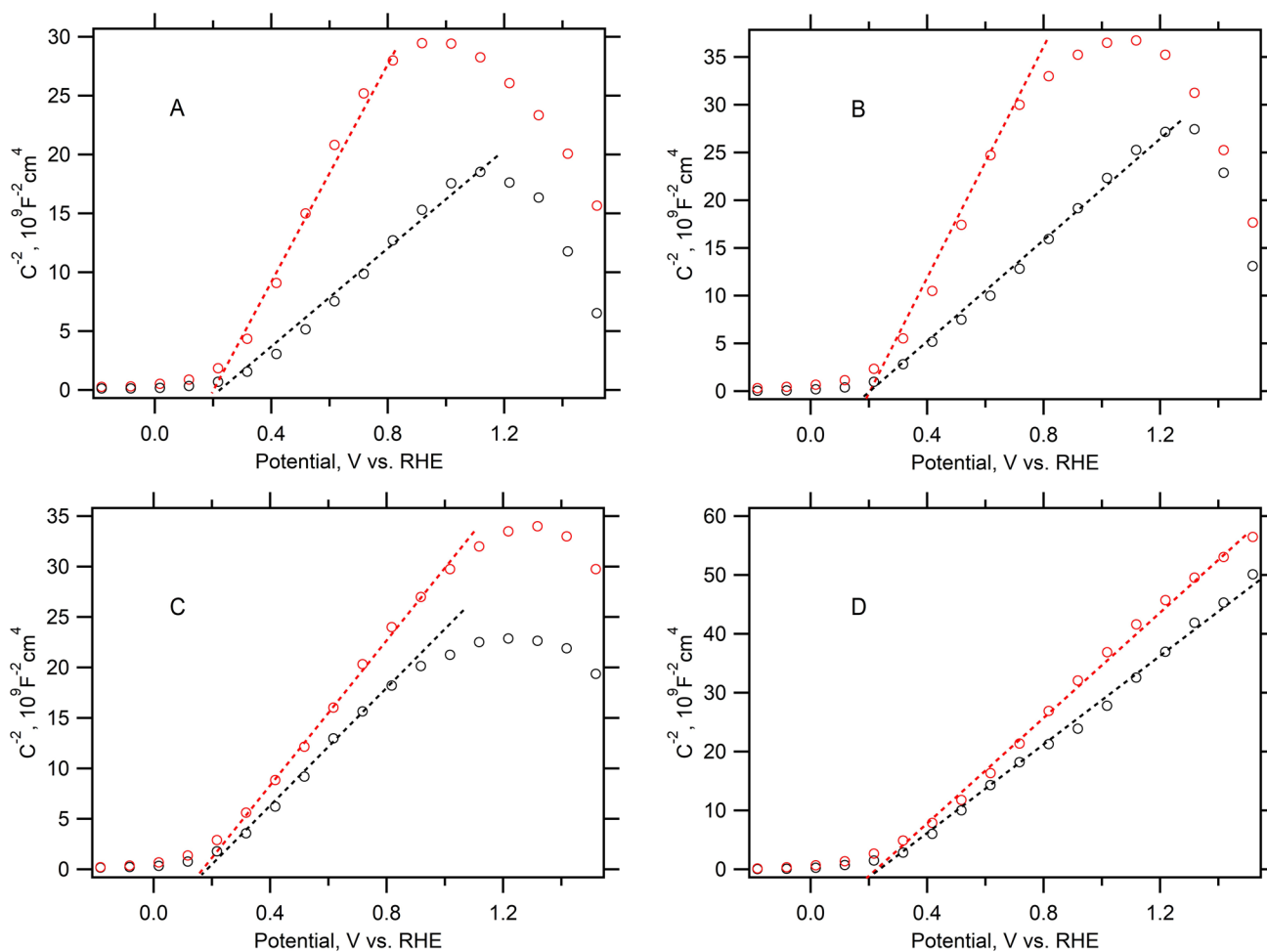
Fig. 5 Mott-Schottky plots for ZnO thin films produced by spray pyrolysis: SP1 (chart **A**), SP2 (chart **B**), SP3 (chart **C**), and SP4 (chart **D**). Black markers (lines) as-prepared film; red markers (lines) the same film after annealing at 450 °C. Electrolyte solution is aqueous 0.5 M KCl saturated with ZnO. Potentials were measured with Ag/AgCl reference electrode and are recalculated against RHE

by spray pyrolysis. This even holds for SP1 films, which contained ≈22% pinholes, see above, and hence, its analysis is unreliable. Blank FTO has $V_{fb} \approx 0.1$ V vs. RHE and $N_D \approx 10^{21}$ cm^{-3} [17, 18]. (FTO shows depletion behavior with a linear Mott-Schottky plot [10, 12], demonstrating that a thin space charge layer could exist even on the degenerate semiconductor.)

The found V_{fb} is equal to the Fermi level position at zero band bending. For V_{fb} expressed against the standard hydrogen electrode (SHE), the corresponding "electrochemical work function," φ_{fb}, equals:

$$\varphi_{fb} = -eV_0^{SHE} + eV_{fb} \qquad (6)$$

where V_0^{SHE} is the potential of SHE in the absolute scale, $V_0^{SHE} \approx -4.44$ V [47]. This approach works reasonably well in the case of TiO$_2$, in which Nernstian dependence of V_{fb} on pH (−59 mV/pH) is proven [12], and the work function is calculated from Eq. 6 for a pH corresponding to the point of zero charge [22]. The latter is reported to be between 8 to 9.5 for ZnO (average value is 8.8) [12]; but it should also be considered that V_{fb} for ZnO thin films are surprisingly insensitive to pH of electrolyte solution. More precisely, the statistical analysis of bulky data (223 entries) gave (−4.8 ± 2.3) mV/pH for ZnO thin films, (−43 ± 15) mV/pH for all morphologies, and (−67 ± 21) mV/pH for all morphologies excluding thin films [12]. By selecting the last value as the most probable one for the ZnO single crystals and assuming the pH$_{PZC} \approx 8.8$ (see above), Eq. 6 provides the electrochemical work functions, φ_{fb}, of 4.11 eV and 4.14 eV for the faces (000$\bar{1}$) and (0001), respectively (i.e., for the O-terminated and Zn-terminated faces, respectively) (Table 4).

Adopting the same evaluation routine for V_{fb} of thin films (from Table 3) provides the corresponding electrochemical work functions, φ_{fb}, for all the as-received and heat-treated
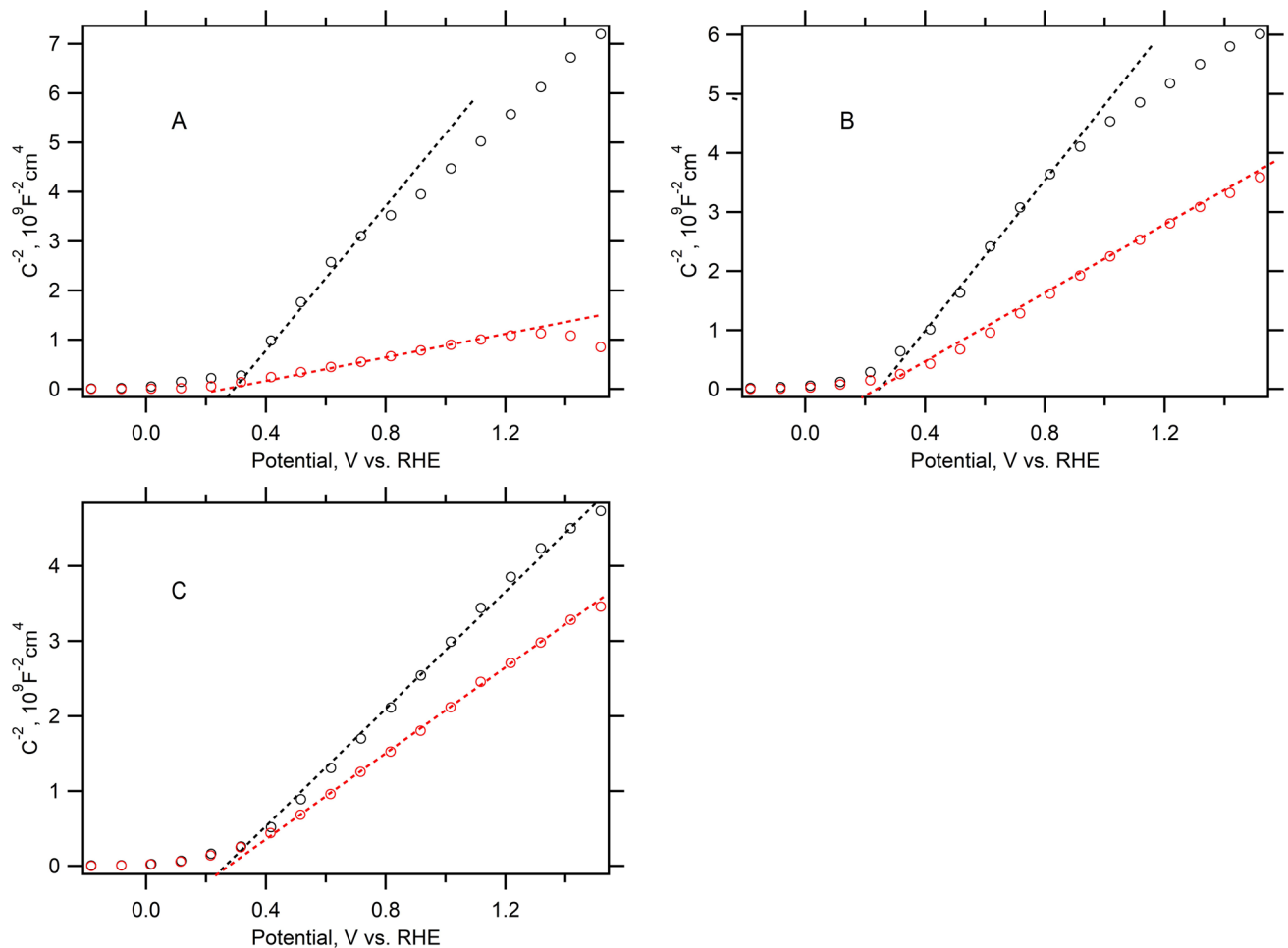
Fig. 6 Mott-Schottky plots for ZnO thin films produced by magnetron sputtering: MS1 (chart **A**), MS2 (chart **B**), and MS3 (chart **C**). Black markers (lines) as-prepared film; red markers (lines) the same film after annealing at 450 °C. Electrolyte solution is aqueous 0.5 M KCl saturated with ZnO. Potentials were measured with Ag/AgCl reference electrode and are recalculated against RHE

ZnO thin films. Table 4 lists the specific data. In summary, the φ_{fb} values of ca. 4.3 eV are obtained for all the SP films and ca. 4.4 eV for all MS films, in all cases nearly independent of the subsequent heat treatment.

Similar values of φ_{fb} were recently reported for ZnO nanorod electrodes (4.4 to 4.6 eV) [45], and the value of 4.6 eV can be also estimated from the "universal average" ($V_{fb} = 0.203$ V) mentioned above [12]. (However, in this case, the experimental pH is unknown for obvious reasons: 223 entries in statistical analysis.) The minimal annealing effect in ZnO resembles the behavior of TiO_2 thin films [19] but differs markedly from SnO_2 thin films, which exhibited a substantial increase in flatband potential (work function) following thermal treatment [19, 20].

Table 3 further presents donor concentrations (N_D) calculated from Eq. 5. Absolute values need to be considered with care, due to uncertainty in physical surface areas, and

the fact the Mott-Schottky analysis tends to overestimate the donor concentrations [12, 20], particularly in materials with a small effective electron mass ($m^* = 0.215 \cdot m_0$ for ZnO [48]). The density of conduction-band states (N_C) in ZnO (wurtzite) is:

$$N_C = 2\left(\frac{2\pi m^* k_B T}{h^2}\right)^{3/2} \cong 2 \cdot 10^{18} cm^{-3} \tag{7}$$

(h is the Planck constant). The offset of Fermi level from the edge of conduction band equals [47]:

$$\zeta_{nb} = \frac{k_B T}{e} ln\left(\frac{N_C}{N_D}\right) \tag{8}$$

Hence, ZnO is expected to be degenerate for $N_D > 2 \cdot 10^{18} cm^{-3}$. This, however, contradicts our finding that good ZnO films provide a rectifying electrochemical interface (cf. Fig. 4). A

Table 3 Data obtained from electrochemical (N_D, V_{fb}) and Kelvin probe (φ_K) measurements of ZnO films on FTO substrates. as-rec, as-received; HT, after heat treatment at 450 °C for 1 h; UV, exposure to UV light (see Experimental Section for details). Reference data for wurtzite single crystal (0001) and (000$\bar{1}$) are also shown

Sample	N_D as-rec [cm^{-3}]	N_D HT [cm^{-3}]	V_{fb} as-rec [V]	V_{fb} HT [V]	φ_K as-rec[a] [eV]	φ_K as-rec/UV[b] [eV]	φ_K (HT)[a] [eV]	φ_K HT/UV[b] [eV]
SP1	$8.8 \cdot 10^{20}$	$3.9 \cdot 10^{20}$	[c]0.22	[c]0.20	4.26	4.66	4.41	4.75
SP2	$6.9 \cdot 10^{20}$	$3.1 \cdot 10^{20}$	[c]0.20	[c]0.20	4.17	4.59	4.28	4.82
SP3	$6.2 \cdot 10^{20}$	$4.7 \cdot 10^{20}$	[c]0.18	[c]0.19	4.18	4.51	4.36	4.76
SP4	$5.1 \cdot 10^{20}$	$4.2 \cdot 10^{20}$	[c]0.21	[c]0.22	4.21	4.86	4.38	5.00
MS1	$2.5 \cdot 10^{18}$	$1.6 \cdot 10^{19}$	[c]0.30	[c]0.30	4.10	4.61	4.36	4.78
MS2	$2.7 \cdot 10^{18}$	$6.6 \cdot 10^{18}$	[c]0.28	[c]0.27	4.18	4.59	4.37	4.77
MS3	$4.5 \cdot 10^{18}$	$6.1 \cdot 10^{18}$	[c]0.26	[c]0.27	4.19	4.45	4.43	4.83
Single cryst. (O-term.)	[d]$2.51 \cdot 10^{18}$	-	[d]0.20	-	4.13	4.54	-	-
Single cryst. (Zn-term.)	[d]$4.79 \cdot 10^{17}$	-	[d]0.23	-	3.99	4.58	-	-

[a]Average value from 500 measurements over 25 min (as in Fig. 7)

[b]Initial value immediately after UV treatment (cf. Fig. 7)

[c]Referred to RHE (pH $\approx$ 5.4–5.9)

[d]Data from Ref. [46]; V_{fb} is referred to RHE (pH = 6.84)

similar paradox follows from many literature values of N_D [11, 12]. More specifically, out of the 190 values of V_{fb}, which were compiled in [12], in only 8 cases, Eq. 8 provided plausible values for ζ_{nb}.

The width of depletion layer (W) equals:

$$W = \left(\frac{2\varepsilon_0 \varepsilon_r}{e N_D} \right)^{1/2} \left(V_{app} - V_{fb} - \frac{k_B T}{e} \right)^{1/2} \quad (9)$$

V_{app} is the applied potential. For the $\approx$1 eV band bending (which is roughly the fitted region in Fig. 6) and $N_D = 2 \cdot 10^{18}$ cm^{-3}, Eq. (9) predicts $W = 21$ nm. This is an estimate for the minimal ZnO film thickness to fully accommodate the space charge layer. This condition is obviously met in all films reported in this study.

Despite absolute values of N_D being uncertain, relative comparison of the two synthetic techniques shows that MS films have significantly lower (by two orders of magnitude) donor concentrations than SP films. Calcination causes a small decrease in N_D for SP films, but an increase for MP films; the effect of annealing is less pronounced for thicker films, which also exhibit broader linearity interval in Mott-Schottky plots (Figs. 5 and 6). We assume that magnetron sputtering produces ZnO films with a lower concentration of defects acting as donors (presumably O-vacancies) because oxygen vacancies in reactively sputtered ZnO films can be compensated by the flux of oxygen atoms (O) created in the ECWR plasma due to O_2 dissociation by collisions with energetic electrons.

Table 4 The electrochemical work functions calculated from flatband potentials of ZnO films on FTO substrates. as-rec, as-received, HT, after heat treatment at 450 °C for 1 h. Reference data for wurtzite single crystal (0001) and (000$\bar{1}$) are also shown

Sample	V_{fb}(pH)[a] [mV/pH]	pH (exp)[b] as-rec	φ_{fb} as-rec [eV]	pH (exp) HT	φ_{fb} HT [eV]
SP1	−4.8	5.6	4.31	5.8	4.28
SP2	−4.8	5.9	4.28	5.8	4.28
SP3	−4.8	5.9	4.26	5.4	4.29
SP4	−4.8	5.4	4.32	5.5	4.33
MS1	−4.8	5.5	4.40	5.9	4.38
MS2	−4.8	5.5	4.38	5.9	4.35
MS3	−4.8	5.8	4.34	5.4	4.38
Single cryst. (O-term.)	−67	[c]6.84	4.11	-	-
Single cryst. (Zn-term.)	−67	[c]6.84	4.14	-	-

[a]pH-dependence of the flatband potential; average value from statistical analysis [12]

[b]The actual pH in the respective experiment (EIS measurement)

[c]Data from Ref [46]

Kelvin probe measurements

Work function was alternatively determined using Kelvin probe measurements on the same ZnO thin films, see Table 3. (These work functions are coded φ_K to distinguish them from electrochemical work functions, φ_{fb} discussed above.) In general, we observe the following trends: (i) φ_K values are similar for SP and MS as-received (as-rec) films but (ii) systematically larger (by ca. 0.1–0.2 eV) for annealed films. The latter finding agrees perfectly with φ_K values reported by Yeh et al. [49] for amorphous and crystalline ZnO grown by pulsed laser deposition, where crystalline films exhibited φ_K values ca. 0.1 eV larger than for amorphous films. In contrast, φ_{fb} values are nearly intact by annealing (Table 3, and Eq. 6).

We also investigated changes in φ_K caused by UV irradiation in air (Fig. 7). In general, in all cases, work function values were markedly enhanced by UV excitation, with the effect persisting for > 10 min after switching off the UV light. Photoexcitation of ZnO in air reportedly causes chemisorption of ionic oxygen through the reaction of photogenerated electrons [50]. The observed enhancement in work function in UV-activated ZnO is reminiscent of the same behavior of SnO_2 and ITO [49] but opposite the behavior of nanocrystalline TiO_2 thin films [51, 52]. In titania films, Kelvin probe measurements indicated a drop in work function with a markedly faster relaxation to initial values over several minutes. This was attributed to recombination of photogenerated charge carriers and slow diffusion (trapping/de-trapping) of electrons through the network of TiO_2 nanoparticles [52].

In the reported compact ZnO films, effects at grain boundaries are assumed to be less important thanks to the dense morphology of nanocrystals and to the higher carrier mobility of ZnO compared to TiO_2. Obviously, UV activation of ZnO and its relaxation cannot be explained by slow electron diffusion in a polycrystalline skeleton. This is corroborated by a model experiment on ZnO (wurtzite) single crystal, in which the particle–particle charge transfer is naturally absent. Yet, the single crystal still exhibits a significant enhancement in φ_K with UV treatment: from 4.13 to 4.54 eV (for O-terminated wurtzite crystal) or from 3.99 to 4.58 eV (for Zn-terminated wurtzite crystal); see Table 3.

Notably, values for ZnO single crystal agree with the measurements of flatband potentials of the same faces of ZnO single crystal after photoetching under an anodic bias [46]. The observed enhancement of φ_K of the as-received crystals (by 0.04 V for O-terminated face compared to the Zn-terminated face) is not reproduced by electrochemical work functions, φ_{fb}, of the same faces, exhibiting decrease by 0.03 eV (see above and [46]). Nevertheless, the trend of electrochemical and Kelvin probe work functions is identical, if we consider the φ_K values

for the UV-treated single crystals (Table 3). In this case, the φ_K and φ_{fb} values equal 4.54 and 4.11 eV, respectively, for the O-terminated face and 4.58 and 4.14 eV, respectively, for the Zn-terminated face. The rationale for this observation is that Zhang et al. [46] actually reported their V_{fb} values for crystals, which were subjected to photoetching prior to their Mott-Schottky measurement. They noted that photoetching removes deep surface states in the band gap of ZnO, which could result in non-linear Mott-Schottky plots [46].

A similar study of SnO_2 and ITO reported a consistent increase in φ_K (by 0.4–0.5 eV) following UV/ozone treatment and attributed it to removal of near-surface oxygen vacancies [49]. This effect was not permanent, as after re-equilibration with air, the film released oxygen, while O-vacancies reappeared. This effect was reproduced with the reported ZnO films, where φ_K values for UV-treated samples (Table 3) returned to their original values within several weeks of storage in ambient conditions (data not shown).

Data reported here, together with earlier literature, illustrate the rich complexity of problems associated with the measurement of the electronic structure of ZnO thin films near the conduction band minimum. In general, Kelvin probe measurements made in air specifically highlight the effect of annealing. It can be hypothesized that annealing in air decreases the number of oxygen vacancies near the surface (similarly to the UV-effect discussed in the previous paragraph), thus decreasing the concentration of free electrons in the conduction band. This enhances the offset of Fermi level from the conduction-band minimum, i.e., increases the work function [53]. On the other hand, at the electrochemical interface, the dominating mechanism controlling the Fermi level position is the effect of double-layer on the ZnO surface, e.g., the surface dipole associated with orientation of water molecules [12] or their dissociative adsorption [22]. We also note that annealing of the reported ZnO films does not significantly influence the crystallinity of the layers (see Fig. 3 and discussion thereof), which qualitatively supports the assumption that, in general, interfacial effects are primarily responsible for the control of Fermi level position (work function).

Photoelectrochemistry

Figure 8 shows photoelectrochemical current/voltage plots under intermittent UV irradiation. Unusually large photocurrents are observed in fresh ZnO films, which rapidly disappear (already during the first scan), and this attenuation progresses in repeated measurements. We are not aware of reporting this effect in any of the earlier ZnO photoelectrochemical studies [1, 6, 7, 12, 54], though several authors noted an instability in ZnO photoelectrodes. It was attributed to photocorrosion [6, 45], caused by
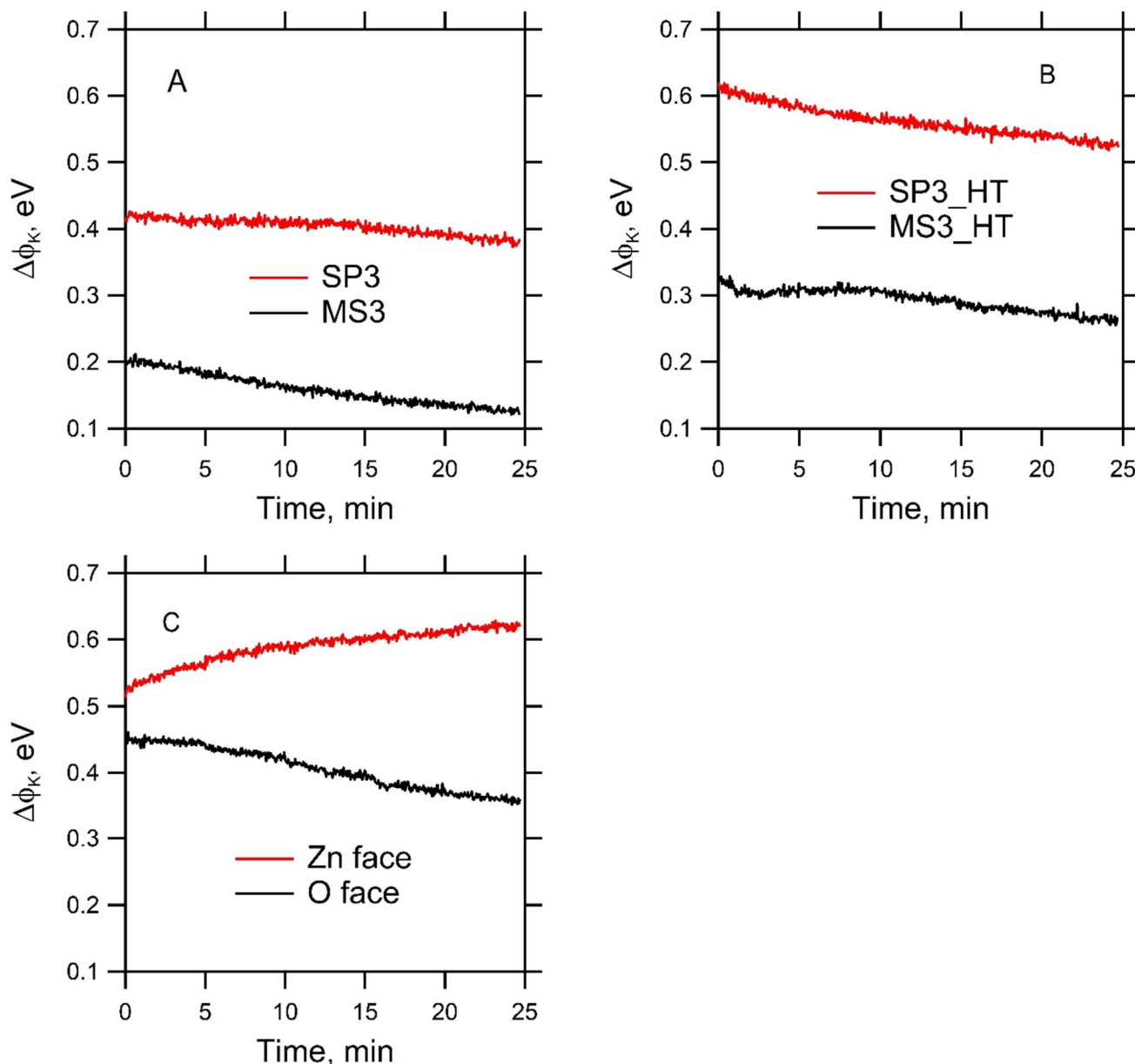
Fig. 7 Relative enhancement of work function caused by UV illumination ($\Delta\varphi_K$). Work function was measured by Kelvin probe on ZnO thin films, of comparable thickness ($\approx$105 nm for SP3 and 110 nm for MS3), deposited on FTO. As-prepared samples (chart **A**). Annealed samples (chart **B**). Chart **C** shows corresponding data for ZnO (wurtzite) single crystals (0001) with two terminations: Zn- or O-face, respectively. Values for $\Delta\varphi_K$ are referenced to the work function of blank (non-illuminated) samples

dissolution of ZnO and O_2 evolution under action of the photogenerated holes (h^+):

$$ZnO + 2h^+ \rightarrow Zn^{2+} + 1/2\ O_2 \qquad (10)$$
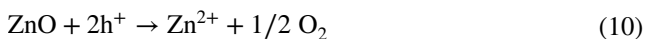
Extreme peak photocurrents, in the order of mA/cm^2 (cf. Fig. 8), were observed for all virgin films (SP1-4 and MP1-3) independent of their preparation and post-calcination history (data not shown). This could be explained by the contribution of charge carriers beyond the space charge region (Gärtner model) in agreement with [32]. A better performance for annealed films was always apparent, but the drop of the initial "super-photocurrent" (cf. Fig. 8) could be caused by simultaneous electrode degradation (cf. Eq. 10). It should be noted that previously studied TiO$_2$ and SnO$_2$ films on FTO provided photocurrents of ca. tens of µA/cm^2 only at the same illumination intensity and with similar experimental conditions [19]. Bakhtiargonbadi

Fig. 8 Linear sweep voltammetry under intermittent UV light. (Upper chart) MS1 sample, (lower chart) SP2 sample (narrow lines, 1st sweep; bold lines, 2nd sweep). Black lines as-received film; red lines the same film after annealing at 450 °C. Photoexcitation is applied with 5 s dark/light intervals. Electrolyte solution is aqueous 0.5 M Na_2SO_4, saturated with ZnO pH 7
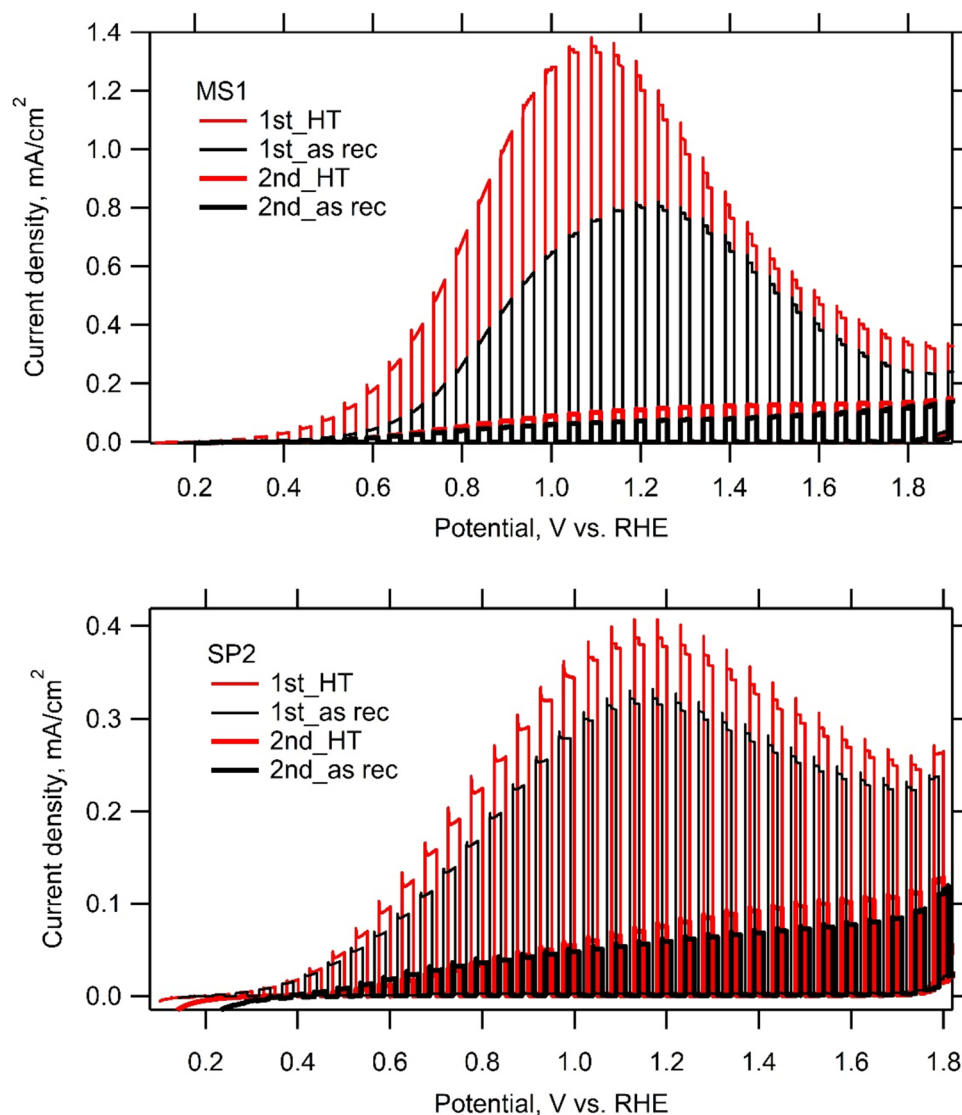
et al. [55] observed photocurrents in range of $\mu A/cm^2$ under simulated sunlight for ZnO thin films fabricated by electrospinning method. Hence, the ZnO thin films reported here obviously appear to be very promising photoelectrochemical materials, if the stability issues are solved.

An alternative explanation of fading of super-photocurrents (Fig. 8) could be the work-function enhancement by UV light (cf. Fig. 7 and discussion thereof). Obviously, both the drop in O-vacancy concentration and the associated drop in conductivity [49], as well as work-function enhancement, would logically impede electrochemical water reduction on photoexcited ZnO. However, the repeated photoelectrochemical testing of our "weeks-relaxed" electrodes did not provide any enhancement in the photocurrent (Fig. S3 in Supporting Info). At this stage of our research, we must leave this question open for deeper studies in the future.

Conclusions

High-quality dense ZnO (wurtzite) thin films (35–120 nm) were prepared by (i) spray pyrolysis (SP) and (ii) pulsed reactive magnetron sputtering combined with radio frequency electron cyclotron wave resonance plasma (MS). Four different substrates were used: FTO, amorphous SiO_2, Si, and Si/SiO_2. For comparison, macroscopic single crystals with either O- termination $(000\bar{1})$ or Zn- termination (0001) were investigated too.

ZnO (wurtzite) crystallite sizes range from 12 to 26 nm, indicating that the thin films consist of $\approx$2–10 monolayers of single crystallites. Crystals are sintered into a virtually non-porous compact body for all MS films (35–110 nm) and for the SP films ($\geq$ 65 nm). These films exhibit nearly ideal rectifying function on an electrochemical interface. On all types of substrates, SP films are more anisotropic. The Si substrate is prone to air oxidation during spray pyrolysis.

Work functions for ZnO/electrolyte interfaces (φ_{fb}) are ≈ 4.3 eV for SP films and ≈ 4.4 eV for MS films. Changes due to annealing are small, if any. Donor concentrations are, by two orders of magnitude, smaller for MS films compared to SP films. This is attributed to quenching of O-vacancies in the ECWR plasma.

Work functions for the ZnO/air interface determined by Kelvin probe (φ_K) are ≈ 4.2 eV for all films but systematically larger (by 0.1–0.2 eV) for annealed films. Work function values are strongly enhanced by UV-excitation (by ca. 0.2–0.6 eV), which persists after switching-off UV illumination. The UV effect is omnipresent in all films including ZnO single crystal.

Photoelectrochemical water oxidation demonstrated unusually large photocurrents on both MS- and SP- virgin films. The subsequent fading of photocurrents is discussed in terms of photocorrosion and work function changes by O-vacancies.

Declarations

Competing interests The authors declare no competing interests.

References

1. Borysiewicz MA (2019) ZnO as a functional material, a review. Crystals 9:505
2. Anta JA, Guillet F, Tena-Zaera R (2012) ZnO-based dye-sensitized solar cells. J Phys Chem C 116:11413–11425
3. Zhang P, Wu J, Zhang T, Wang Y, Liu D, Chen H, Ji L, Liu C, Ahmad W, Chen ZD, Li S (2018) Perovskite solar cells with ZnO electron-transporting materials. Adv Mater 30:1703737
4. Izzi M, Sportelli MC, Torsi L, Picca RA, Cioffi N (2023) Synthesis and antimicrobial applications of ZnO nanostructures: a review. ACS Appl Nano Mater 6:10881–10902
5. Wang L, Zhang G, Liu Q, Duan H (2018) Recent progress in Zn-based anodes for advanced lithium ion batteries. Mater Chem Front 2:1414–1435
6. Dworschak D, Brunnhofer C, Valtiner M (2020) Photocorrosion of ZnO single crystals during electrochemical water splitting. ACS Appl Mater Interfaces 12:51530–51536
7. Dom R, Kim HG, Borse PH (2014) Efficient hydrogen generation over (100)-oriented ZnO nanostructured photoanodes under solar light. Cryst Eng Comm 16:2432–2439
8. Zhao Y, Niu Z, Zhao J, Xue L, Fu X, Long J (2023) Recent advancements in photoelectrochemical water splitting for hydrogen production. Electrochem Energy Rev 6:14
9. Suryavanshi RD, Mohite SV, Bagade AA, Shaikh SK, Thorat JB, Rajpure KY (2018) Nanocrystalline immobilised ZnO photocatalyst for degradation of benzoic acid and methyl blue dye. Mater Res Bull 101:324–333
10. Hankin A, Bedoya-Lora FE, Alexander JC, Regoutz A, Kelsall GH (2019) Flat band potential determination: avoiding the pitfalls. J Mater Chem A 7:26162–26176
11. Sivula K (2021) Mott-Schottky analysis of photoelectrodes: sanity checks are needed. ACS Energy Lett 6:2549–2551
12. Patel MY, Mortelliti MJ, Dempsey JL (2022) A compendium and meta-analysis of flatband potentials for TiO$_2$, ZnO, and SnO$_2$ semiconductors in aqueous media. Chem Phys Rev 3:011303
13. Douloumis A, Vrithias NRE, Katsarakis N, Remediakis IN, Kopidakis G (2022) Tuning the workfunction of ZnO through surface doping with Mn from first-principles simulations. Surf Sci 726:122175
14. Saikumar AK, Sundaresh S, Nehate SD, Phelps J, Abdolvand R, Sundaram KB (2023) Work function estimation of gallium-doped zinc oxide using transparent gate electrode MOSFET. ECS J Solid State Sci Technol 12:033010
15. Kyu Kang S, Yun Kang D, Wan Park J, Rock Son K, Geun Kim T (2021) Work function-tunable ZnO/Ag/ZnO film as an effective hole injection electrode prepared via nickel doping for thermally activated delayed fluorescence-based flexible blue organic light-emitting diodes. Appl Surf Sci 538:148202
16. Claeyssens F, Freeman CL, Allan NL, Sun Y, Ashfold MNR, Harding JH (2005) Growth of ZnO thin films—experiment and theory. J Mater Chem 15:139–148
17. Kavan L, Tetreault N, Moehl T, Grätzel M (2014) Electrochemical characterization of TiO$_2$ blocking layers for dye sensitized solar cells. J Phys Chem C 118:16408–16418
18. Moehl T, Suh J, Severy L, Wick-Joliat R, Tilley SD (2017) Investigation of (leaky) ALD TiO$_2$ protection layers for water-splitting photoelectrodes. ACS Appl Mat Interfaces 9:43614–43622
19. Zlamalova M, Mansfeldova V, Tarabkova H, Krysova H, Kavan L (2023) Variable work function of semiconducting thin-film oxide electrodes: a case study of SnO$_2$ and TiO$_2$. J Solid State Electrochem 27:1935–1943
20. Kavan L, Steier L, Grätzel M (2017) Ultrathin buffer layers of SnO$_2$ by atomic layer deposition: perfect blocking function and thermal stability. J Phys Chem C 121:342–350
21. Windish JA, Exarhos GJ (2000) Mott-Schottky analysis of thin ZnO films. J Vac Sci Technol A 18:1677–1680
22. Mansfeldova V, Zlamalova M, Tarabkova H, Janda P, Vorokhta M, Piliai L, Kavan L (2021) Work function of TiO$_2$ (anatase, rutile, and brookite) single crystals: effects of the environment. J Phys Chem C 125:1902–1912
23. Nematov DD, Kholmurodov KT, Husenzoda MA, Lyubchyk A, Burhonzoda AS (1922) Molecular adsorption of H$_2$O on TiO$_2$ and TiO$_2$: Y surfaces. J Human Earth Future 3:213–222
24. Deak P, Kullgren J, Aradi B, Frauenheim T, Kavan L (2016) Water splitting and the band edge positions of TiO$_2$. Electrochim Acta 199:27–34
25. Jeong S, Seo S, Park H, Shin H (2019) Atomic layer deposition of a SnO$_2$ electron-transporting layer for planar perovskite solar

cells with a power conversion efficiency of 18.3%. Chem Commun 55:2433–2436

26. Lee Y, Lee S, Seo G, Paek S, Cho KT, Huckaba AJ, Calizzi M, Choi DW, Park JS, Lee D, Lee HJ, Asiri AM, Nazeeruddin MK (2018) Efficient planar perovskite solar cells using passivated tin oxide as an electron transport layer. Adv Sci 5:1800130

27. Kavan L, Vlckova-Zivcova Z, Zlamalova M, Zakeeruddin SM, Grätzel M (2020) Electron-selective layers for dye-sensitized solar cells based on TiO_2 and SnO_2. J Phys Chem C 124:6512–6521

28. Lieberman MA, Lichtenberg AJ (2005) Principles of plasma discharges and materials processing. Wiley

29. Khadayeir AA, Wannas AH, Yousif FH (2022) Effect of applying cold plasma on structural, antibacterial and self cleaning properties of α-Fe_2O_3 (HEMATITE) thin film. Emerg Sci J 6:75–85

30. Novák P, Nedvědová L, Kozák T, Šotová P, Bláhová O, Jansa Z, Medlín R, Frank Netrvalová M, Minár J (2023) Investigation of carrier transport in ZnO and ZnO: Al thin films sputtered at different oxygen conditions. Thin Solid Films 780:139942

31. Ye W, Fang K (2020) Comparative study on structure and properties of ZnO thin films prepared by RF magnetron sputtering using pure metallic Zn target and ZnO ceramic target. Surf Eng 36:49–54

32. Zhang W, Yan D, Appavoo K, Cen J, Wu Q, Orlov A, Sfeir MY, Liu M (2017) Unravelling photocarrier dynamics beyond the space charge region for photoelectrochemical water splitting. Chem Mater 29:4036–4043

33. Saha JK, Bukke RN, Mude NN, Jang J (2020) Significant improvement of spray pyrolyzed ZnO thin film by precursor optimization for high mobility thin film transistors. Sci Rep 10:8999

34. Hubička Z, Zlámal M, Olejníček J, Tvarog D, Čada M, Krýsa J (2020) Semiconducting p-type copper iron oxide thin films deposited by hybrid reactive-HiPIMS + ECWR and reactive-HiPIMS magnetron plasma system. Coatings 10:232

35. Stranak V, Hubicka Z, Cada M, Bogdanowicz R, Wulff H, Helm CA, Hippler R (2018) Influence of reactive oxygen species during deposition of iron oxide films by high power impulse magnetron sputtering. J Phys D Appl Phys 51:095205

36. Stranak V, Herrendorf A-P, Wulff H, Drache S, Cada M, Hubicka Z, Tichy M, Hippler R (2013) Deposition of rutile (TiO2) with preferred orientation by assisted high power impulse magnetron sputtering. Surf Coat Technol 222:112–117

37. Beerbom MM, Lägel B, Cascio AJ, Doran BV, Schlaf R (2006) Direct comparison of photoemission spectroscopy and in situ Kelvin probe work function measurements on indium tin oxide films. J Electron Spectr Rel Phen 152:12–17

38. Jerkiewicz G (2020) Standard and reversible hydrogen electrodes: theory, design, operation, and applications. ACS Catal 10:8409–8417

39. Krysova H, Neumann-Spallart M, Tarabkova H, Pausová S, Janda P, Maixner J, Kavan L, Krysa J (2021) Reconstruction of SnO_2 after cathodic polarization of FTO films - a simple way of fabricating orthorhombic SnO_2. MaterChemPhys 273: 125038

40. Steier L, Luo J, Schreier M, Mayer MT, Sajavaara T, Grätzel M (2015) Low-temperature atomic layer deposition of crystalline and photoactive ultrathin hematite films for solar water splitting. ACS Nano 9:11775–11783

41. Čada M, Hubička Z, Adámek P, Ptáček P, Šichová H, Šicha M, Jastrabık L (2003) Investigation of RF and DC plasma jet system during deposition of highly oriented ZnO thin films. Surf Coat Technol 174–175:627–631

42. Hassan ES, Abd AN, Dawood MO (2018) The sputter time duration effect on the structural and optical properties of zinc oxide by RF magnetron sputtering. Silicon 10:2901–2906

43. Chen Y, Sun P, Gao C, Yang T, Huang Q (2020) Growth and characterization of c-axis titled ZnO thin film by radio frequency magnetron sputtering. Mater Express 10:53–61

44. Quarto FD, Franco FD, Miraghaei S, Santamaria M, La Mantia F (2017) The amorphous semiconductor Schottky barrier approach to study the electronic properties of anodic films on Ti. J Electrochem Soc 164:C516–C525

45. Guler AC, Antos J, Masar M, Urbanek M, Machovsky M, Kuritka I (2023) Comprehensive evaluation of photoelectrochemical performance dependence on geometric features of ZnO nanorod electrodes. Nanoscale Adv 5:3091–3103

46. Zhang B, Wang Z, Huang B, Zhang X, Qin X, Li H, Dai Y, Li Y (2016) Anisotropic photoelectrochemical (PEC) performances of ZnO single-crystalline photoanode: effect of internal electrostatic fields on the separation of photogenerated charge carriers during PEC water splitting. Chem Mater 28:6613–6620

47. Bisquert J, Cendula P, Bertoluzzi L, Gimenez S (2014) Energy diagram of semiconductor/electrolyte junctions. J Phys Chem Lett 5:205–207

48. Zhang ZH, He M, Li Q (2009) Obtaining the effective electron mass from valence electron energy-loss spectroscopy. Solid State Commun 149:1856–1859

49. Yeh TC, Zhu Q, Buchholz DB, Martinson AB, Chang RPH, Mason TO (2015) Amorphous transparent conducting oxides in context: work function survey, trends, and facile modification. Appl Surf Sci 330:405–410

50. Jacobs CB, Maksov AB, Muckley ES, Collins L, Mahjouri-Samani M, Ievlev A, Rouleau CM, Moon JW, Graham DE, Sumpter BG, Ivanov IN (2017) UV-activated ZnO films on a flexible substrate for room temperature O and H_2O sensing. Sci Rep 7:6053

51. Torras-Rosell A, Johannsen SR, Dirscherl K, Daviethsdottir S, Jeppesen CS, Louring S, Andersen IH (2017) Comparing the photocatalytic activity of TiO_2 at macro- and microscopic scales. Environ Sci Pollut Res Int 24:12683–12690

52. Henning A, Gunzburger G, Johr R, Rosenwaks Y, Bozic-Weber B, Housecroft CE, Constable EC, Meyer E, Glatzel T (2013) Kelvin probe force microscopy of nanocrystalline TiO_2 photoelectrodes. Beilstein J Nanotechnol 4:418–428

53. Drewelow G, Reed A, Stone C, Roh K, Jiang Z-T, Truc LNT, No K, Park H, Lee S (2019) Work function investigations of Al-doped ZnO for band-alignment in electronic and optoelectronic applications. Appl Surf Sci 484:990–998

54. Ahn K-S, Yan Y, Lee S-H, Deutsch T, Turner J, Tracy CE, Perkins CL, Al-Jassim M (2007) Photoelectrochemical properties of N-incorporated ZnO films deposited by reactive RF magnetron sputtering. J Electrochem Soc 154:B956–B959

55. Bakhtiargonbadi F, Esfahani H, Moakhar RS, Dabir F (2020) Fabrication of novel electrospun Al and Cu doped ZnO thin films and evaluation of photoelectrical and sunlight-driven photoelectrochemical properties. Mater Chem Phys 252:123270